High optical storage density using three-dimensional hybrid nanostructures based on machine learning

Dekun Yang[#a], Zhidan Lei[#a], Lijie Li[b], Wei Shen[a], Hui Li[a*], Chengqun Gui[a*], Yi Song[a*]

[#]Dekun Yang and Zhidan Lei contributed equally to this work

[a]The Institute of Technological Sciences, Wuhan University, Wuhan 430072, China

[b]College of Engineering, Swansea University, Bay Campus, Swansea, SA1 8EN, UK

Abstract

The quality of optical storage is determined by several factors, especially diffraction limit, storage media, recording dimensions and readout schemes. To increase the storage density, more progressive strategies reaching high storage density need be explored, including excellent storage media, multiple recording dimensions and robust readout schemes. In this work, the three-dimensional hybrid nanostructures are proposed, which are composed by Si and Si_3N_4. It can be fabricated with the three dimensional (3D) lithography technology, which is able to encode high density data information within multi-dimensions. To obtain robust information readout, spectra with a broad wavelength range and with a large angle range are combined for a high sensitivity. Meanwhile an artificial neural network is used to translate the spectra to the data sequences. For a 4-unit nanostructure, the 27 data sequences with 20% spectral noise, a 100% readout accuracy can be achieved. High readout speed is also demanded in optical storage. Therefore, we reduced the number of the selected wavelengths and angles in the spectra. It is demonstrated that when the number reduces to 1/50 of the original number, the reading accuracy is still 99.7% compared to the full range. Furthermore, the possibility of achieving higher storage densities is investigated for a further study.

Keyword: High density optical storage; Nanostructures; Deep learning; 3D lithography

1 Introduction

"Big data" era stimulates rapid development of optical information storage rather than magnetic storage, owing to the advantages of long performance life, high storage density and low cost [1,2]. Currently, optical disk accounts for the majority of optical storage in our society, such as compact disc, digital video disc, blu-ray disc [3,4]. The recording media of the discs stores one bit per diffraction limited area. Despite significant improvement in storage density, the theoretical storage capacity of the disc can only reach several terabytes due to the diffraction limit [5]. To solve this critical issue, several strategies aimed at increasing storage density are explored. For instance, recording media material-dependent (multi-wavelength and multi-level storage [6,7], two-photon excitation [8], fluorescent nanocrystal [9]), encoding patterns-dependent (polarization-sensitive [10]), readout scheme-dependent (DNA-based [11]) and volume product-dependent (holographic memory [12]). However, each technical route has its own shortcomings. Some of them are difficult to source suitable storage media (multi-wavelength and multi-level storage, two-photon excitation, fluorescent nanocrystal), while others require precise patterning and sophisticated readout scheme (polarization-sensitive, DNA-based) or comprehensive industrialization solutions (holographic memory).

Photonic nanostructures are regarded as another potential technology to obtain higher storage density due to their capability of controlling light at nanometer scale [13]. Interaction between light and matter, such as localized surface plasmons (LSPs) [14,15] and Mie-resonances [16,17], produces

structural colors covering a wide spectrum. Hence researchers can work on encoding information through the wide scattering spectra, which are induced from plasmonic nanostructures [18–20]. To further broaden the scattering spectrum, the polarization-sensitive nanostructures are developed based on Mie-resonances [21]. It can reach near-zero scattering via changing the polarization of incident light, making it possible to further increase the storage density. And yet, an innate critical problem of plasmonic nanostructures is that similar optical responses may be produced from different structures [22]. It brings higher accuracy requirements to readout strategies [23]. Sample fabrication errors and measurement noise can further complicate this problem. Some drawbacks stem from the metal material itself of plasmonic nanostructures. One example is the most common plasmonic material, gold, which can not be encoded with the wavelengths shorter than ~520 nm due to the limitation of interband transitions [24]. As a consequence, the storage density is reduced to a certain extent, compared with full range wavelengths.

To overcome these drawbacks, the strategy based on dielectric nanostructures is proposed to encode data information. One example is silicon, as earth-abundant, environmentally friendly material, it is the most suitable candidate material due to the characters of high refractive index and strong resonant [16,25,26]. In 2019, Peter R developed silicon nanostructures to encode data information based on deep learning via continuous wavelengths and RGB color [24]. They demonstrated that the encoding capacity of this nanostructures can reach up to 9 bits. However, the nanostructures were arranged in two-dimension (2D), which cannot fully utilize the three-dimensional (3D) space due to the fabrication limitation of electron-beam lithography (EBL). In this work, we propose a novel scheme for silicon nanostructures based on 3D lithography, enabling encode data information in three-dimension.

To accurately reconstruct stored data information, the machine-learning approach is used in readout process. The artificial neural network (ANN) is chosen to analyze the spectra scattering from the height changing nanostructures. Since ANNs are good at solving problems that are difficult to be solved analytically or numerically, they are widely applied in many areas, for instance in prediction, classification and pattern recognition [27]. However, except for a few recent examples, ANN is rarely applied to nano-optics, especially in optical storage. In two examples, data classification for holographic memory [28] and scattering spectra analysis [24] for optical storage were accomplished using ANN. In architecture of ANN used in this work, the input corresponds to the simulated scattering spectra of each nanostructure, and the output corresponds to the encoded data sequence. We demonstrate that in the condition of wavelength-depended with a 20% spectral noise, the ANN reach 100% readout accuracy for encoding 27 data sequences. To eliminate issue of the polarization spectrum consistency, one recording strategy that combines wavelength- and angle-dependent is proposed. Furthermore, the limitation of its required spectra volume and the robustness to higher storage densities are studied.

2 Data information encoding and readout

2.1 Nanostructures for data information encoding

As a maskless lithography technology, laser direct writing has the advantage of customized processing and is widely used in the field of micro-nano processing, especially 3D lithography. First of all, we need to verify the hypothesis of whether patterns of different grayscales can produce unique spectral responses, which is the key to realize optical storage. In the experiment, four samples with different grayscale are fabricated using the laser direct writing device (PICOMASTER 100, 4PICO Co., Netherlands) with the laser of 300 nm minimum spot and 405 nm wavelength. The photoresist used for exposure is AZ4562 positive photoresist, suitable for applications requiring coating thicknesses over 3

μm (the surface smoothness measurement results using the 3D profiler are shown in in supplementary Fig. S1a). We imported the model of the experimental sample into diffractMOD of Rsoft software to simulate the spectral response of each structure. The wavelength-dependent spectra are distinctly different from each other in X- and Y-polarizations, which is provided in supplementary Fig. S1b. This phenomenon provides evidence to achieve high density optical storage using 3D lithography.

To verify the hypothesis and solve the problem of weak anti-aging performance of photoresist, the nanostructures are designed using Si family materials. As schematically shown in Fig. 1a, Si_3N_4 is deposited as a thin film on silicon-on-insulator (SOI) substrate that is divided into two equal units (1 μm in length and width). In lithography process, the gray scale (height) change in the Z-axis direction is realized by controlling the energy of the exposure dose between two units. As a consequence, the lithography patterns will be transferred to the Si_3N_4 and Si layers by etching. In this process, to increase spectral signal discrimination of symmetric arrangements, the Si_3N_4 layer in unit 2 is preserved.

As illustrated in Fig. 1b, the thickness of the silicon layer on the SOI substrate is 300 nm, on which a layer of Si_3N_4 with a height of 100 nm has been deposited. We imported the model into Rsoft software to simulate the spectral response of each structure. In this model, the incident angle of the light source is perpendicular to the structure, and the wavelength range is 200 nm-2000 nm, which can be achieved by ordinary light sources such as xenon lamps. Different etch depths (100 nm, 200 nm, 300 nm) for Si layer in unit 1 produce distinct wavelength-dependent spectra in X- and Y-polarized states (Fig .1c). The phenomenon indicates that the use of spectra produced by etching depth-varying nanostructures to encode digital information is a feasible solution.

To further increase the storage density, the three-unit arrangement is used to encode three data sequences as shown in Fig. 2. Therefore, this arrangement provides the nanostructure with the ability to record data information in 3D (X Y Z direction). If the Si layer in certain unit (unit 1-3) is etched down 100 nm, the data is set to '1', otherwise it is '0'. For every 100 nm increase in the etching depth, the data value is added one, such as 200 nm-etching is '2', 300 nm-etching is '3'. The coding rule is arranged from unit 1 to unit 3 to form a data sequence. In this scheme, the storage capacity of 100 nm- and 200 nm-etching can reach up to 8 and 27, respectively.

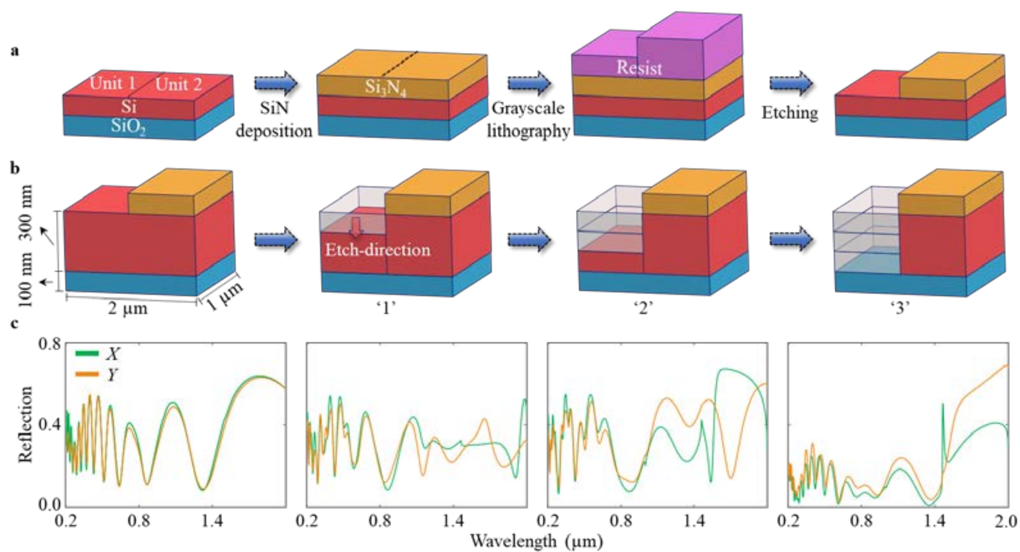

Fig. 1 Illustration of fabrication process and encoding strategy. **a** fabrication process flow for the nanostructure, **b** the etching depth of the Si layer varies according to the grayscale, **c** wavelength-dependent spectra of different etching depth.

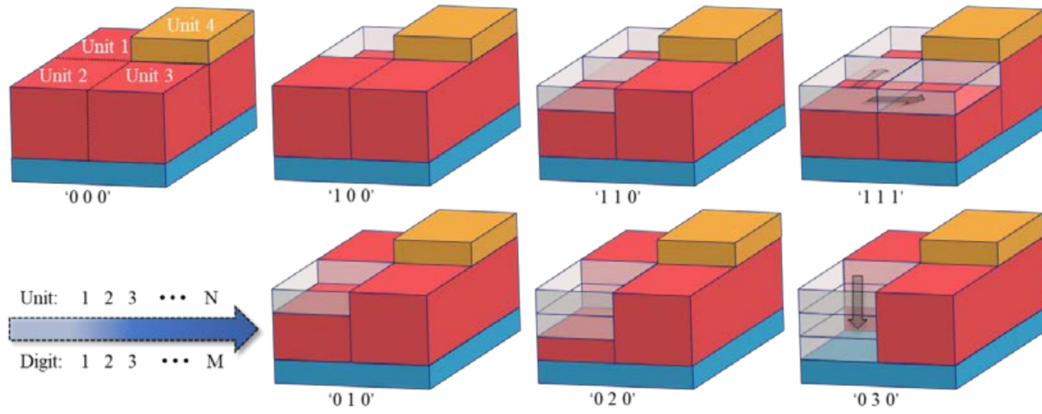

Fig. 2 Description of encoding method: three-unit arrangement is used to encode through X Y Z direction; certain unit (unit 1-3) is etched down by 100 nm, the data is set to '1', otherwise it is '0', after every 100nm increase in etching depth, the digit increases by 1 (encoding from unit 1 to unit 3).

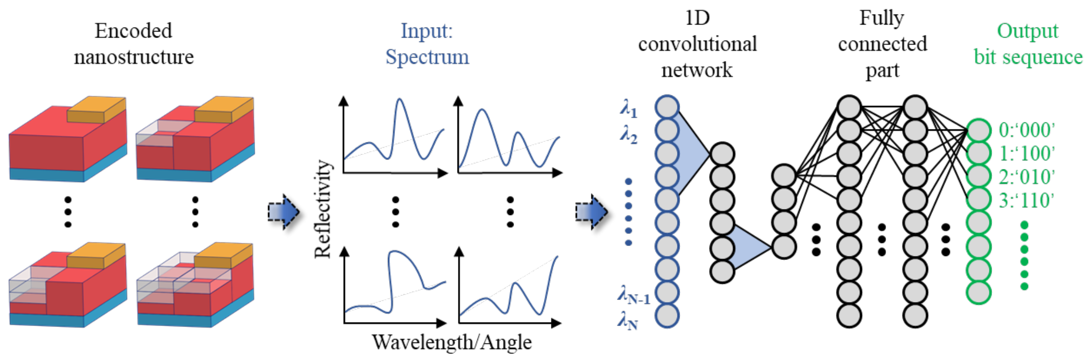

Fig. 3 Sketch of 1D convolutional ANN

2.2 Machine learning based digital information readout

The purpose of the readout is to retrieve the data encoded by the geometries via identifying the spectra information. In this work, we propose a machine-learning method to read out data sequences. As illustrated in Fig. 3, the ANN we employ is a convolutional neural network (CNN), matching to a fully connected network. The CNN are composed of three layers with the 'leaky ReLU' activation function, which has huge superiority for solving pattern recognition problem [29]. In first layer CNN, each channel has 32 filters with a kernel size of 7. Both the second and third layers have 32 and 1 filters with the kernel sizes of 5 and 3, respectively. Each layer in CNN is connected to a max-pooling layer with a kernel size of 2 and a batch normalization. The fully connected network employs "tanh" activations and consists of two layers with 64 and 32 neurons, respectively. Introduce the spectra consisting of X or Y-polarizations into the ANN input layer as parallel channels, each channel uses a kernel of size 7. In the output layer of ANN, each data sequence is assigned to a neuron.

In the training stage of ANN, the spectra of X or Y-polarizations are introduced into the ANN input layer as parallel channels, the encoded data for different geometries are fed into the output layer. We train ANN using 300 wavelength-dependent spectra, which is generated by simulation software. The ratio of the number of spectra for training to testing is set to 7:3. In the readout scheme, the spectra is fed into the trained ANN and forward-propagated through the network to retrieve the data encode by structures. Next, we use the cross-entropy loss and the validation accuracy to evaluate training quality.

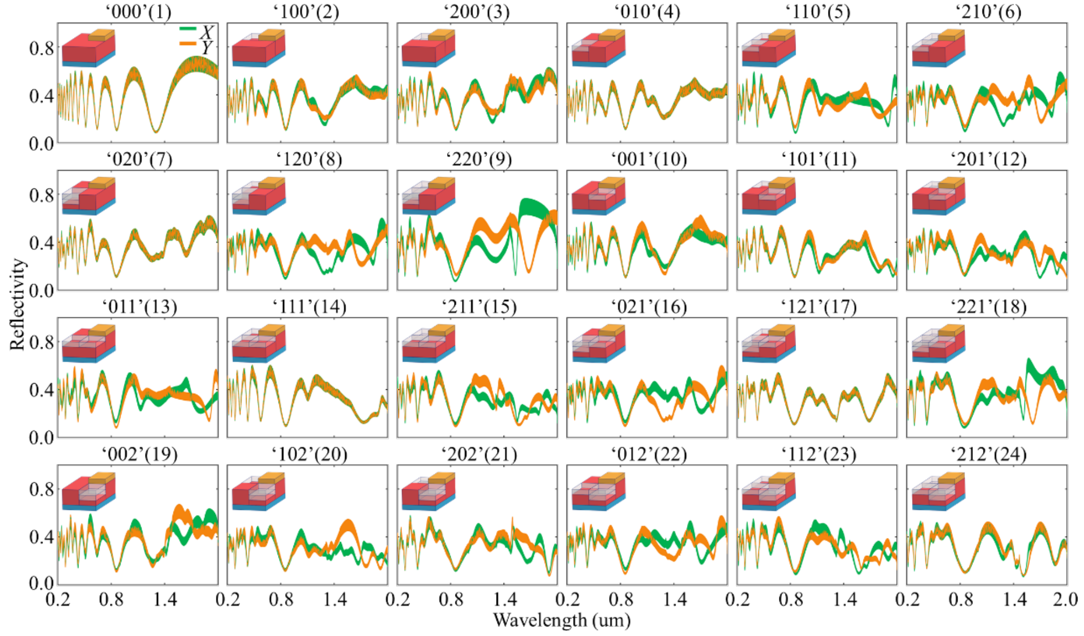

Fig. 4 Simulated wavelength-dependent spectra for 24 data sequences (encoding from unit 1 to unit 3).

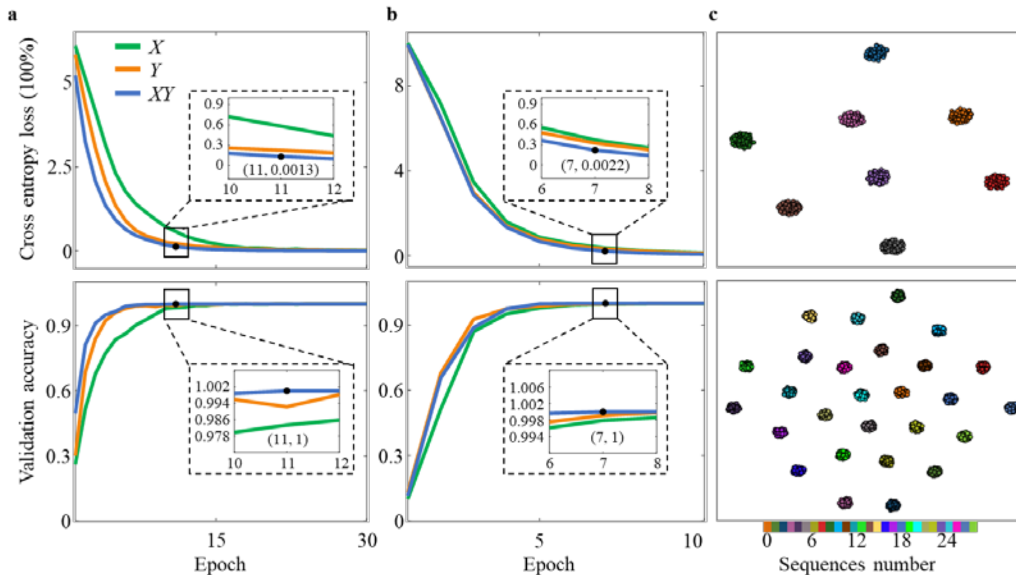

Fig. 5 Training quality and readout accuracy of the ANN trained on full wavelength-dependent spectra. **a** cross entropy loss and validation accuracy of training for 8 data sequences using X-polarization, Y-polarization and XY-polarizations respectively, **b** cross entropy loss and validation accuracy of training for 27 data sequences, **c** t-SNE plot of the XY polarization training sets for 8 and 27.

3 Analysis and estimation of the digital information readout performance

3.1 X- and Y-polarized spectra based on wavelength

Within the 20% spectral noise of the original spectrum, 300 spectra are randomly generated for 27 structure (300 nm-etching) as the wavelength varies from 200 nm to 2000 nm to provide the training set for AAN, 24 of which are shown in Fig. 4. Due to the 20% spectral noise is added, 300 spectra scattered within a reflectivity interval, one 10% noise is used to compensate for fabrication errors and the remaining 10% is to simulate measurement noise. The reasonability of the 20% spectral noise will be discussed in section 3.3. The green line represents the X-polarization and the orange line is for the Y-

polarization. It is noted that the spectral responses of most structures differ significantly between X and Y polarized conditions except for a few cases, such as encoded data sequences '000', '010', '020', '101', '111', '212'. The phenomenon can be attributed to the fact that these structures are symmetrical about the center, with the same spectral sensitivity in both X and Y directions.

The cross entropy loss and the validation accuracy rate of the network trained on the 8 (100 nm-etching) and 27 (200 nm-etching) data sequences at different polarization conditions are shown in Fig. 5a and Fig. 5b, respectively. As the training epoch increases, training with XY-polarizations converges faster than with them alone. In the training of 8 data sequences using XY-polarizations, 100% validation accuracy rate is obtained in the 11th epoch, and the corresponding loss is 0.0013, as shown in Fig. 5a. On the contrary, the convergence rate of 27 data sequences is faster than that of 8, and the accuracy rate reaches 100% in the 7th epoch with the loss of 0.0022. The main reason for this result is that the proportions of symmetric structures are different in the two data sets. Four symmetric structures ('000', '010', '101', '111') are in 100 nm-etching (8 data sequences), whereas only five ('020', '121', '202', '212', '222') are added in 200 nm-etching (27 data sequences). This means that the encoded data with only single-channel information (X-polarization and Y-polarization are the same) accounts for a higher proportion of the 8 data sequences, which reduces the quality of training. In the actual test process, once the validation accuracy reaches 100%, the corresponding readout accuracy is 100%. This is because the training and test sets (spectra) are generated within the same 20% spectral noise, and the number of the training set is sufficient.

To evaluate the distinctiveness of different structures, the t-SNE (t-distributed stochastic neighbor embedding) is used to analyze the data sequences [30]. In t-SNE scatterplot, well-separated scatter points represent clearly distinguishable structures in the data sequences, while adjacent and overlapping points mean very similar data. The results of 8 and 27 data sequences under the XY polarizations are shown in Fig. 5c. Different colors correspond to different structures, and each point represents the simulated spectra with 20% random error. The data sets of all structures are well-separated in the t-SNE plot, which explains why ANN can correctly identify data information with the accuracy of 100%.

3.2 X- and Y-polarized spectra combined wavelength and angle

To achieve 100% readout accuracy with less training epochs, the problem of symmetric structures producing the same spectral response under X and Y polarizations must be solved. In this situation, a recording scheme combining wavelength- and angle-dependent spectra is proposed. Owing to the high refractive index of silicon nanostructures in visible light range [26], the light of 500 nm wavelength is chosen to generate angle-dependent spectra. According to the commonly used objective lens with the numerical aperture of 0.9, the angle range is selected as -64° to 64°.

As illustrated in Fig. 6, the spectral trends under X and Y polarizations are opposite, as the angle of incidence varies between -64° to 64°. Even for symmetric structures ('000', '010', '020', '101', '111', '212'), there is still a clear distinction between the spectra at the two polarization states. This advantage makes up for the symmetry problem of wavelength spectra well. The training results as shown in Fig. 7a, 8 data sequences achieve 100% accuracy in the 8th epoch (corresponding loss: 0.0021) of training, and the 27 data sequences reach the same accuracy in the 5th epoch (corresponding loss: 0.0031). Using spectral information combined with angle and wavelength, the training epoch for two data sets are reduced by 27% and 29%, respectively, compared with using wavelength-dependent spectra alone. In this situation, the well-separated t-SNE plot is shown in Fig. 7b.

To further verify the robustness of this recording scheme, the reduced wavelength- and wavelength

& angle-dependent spectra are trained and tested in ANN. Each spectrum changes from 200 nm to 2000 nm or -64° to 64°, consisting of 1281 data generated in the simulation software. Here the reduced data are selected at a specific step size. The step size varies from 10 to 160 in fixed increments of 10, and the corresponding number of spectra selected from the XY polarization states of angle and wavelength, respectively, are 25, 21, 18, 16, 14, 12, 11, 10, 9, 9, 8, 8. The readout accuracy with the increase of the selection step size is shown in in supplementary Fig. S2.

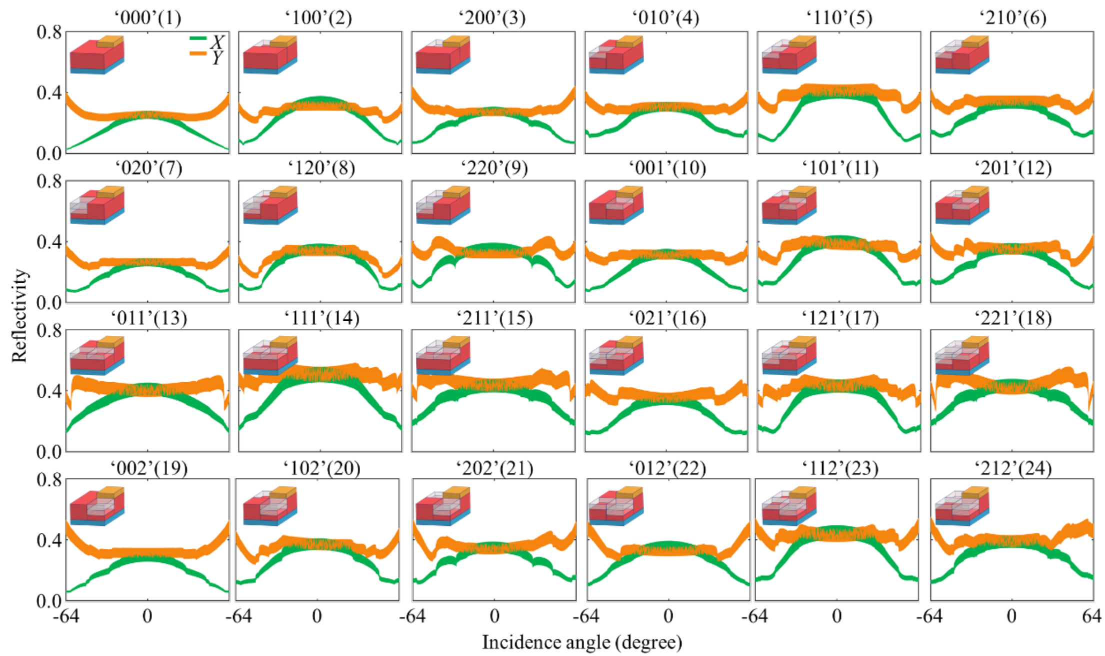

Fig. 6 Simulated angle-depended spectra for 27 data sequences (encoding from unit 1 to unit 3).

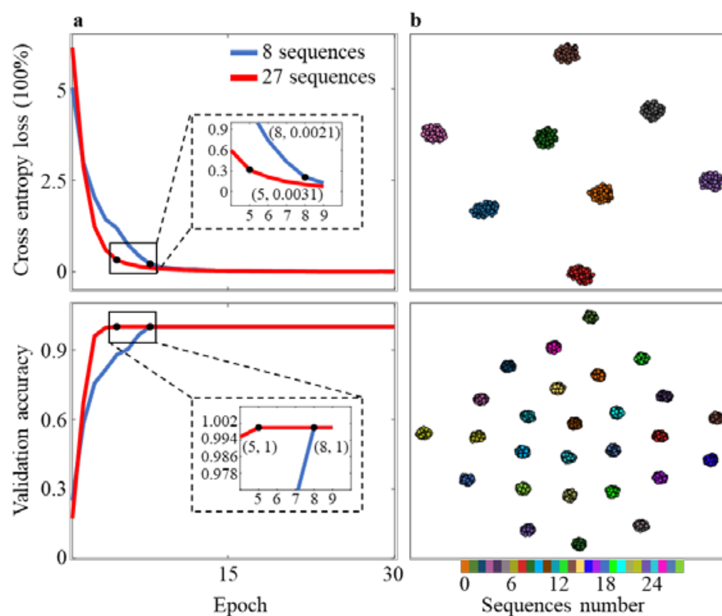

Fig. 7 Training quality and readout accuracy of the ANN trained on full wavelength-dependent spectra for 27 data sequence. **a** cross entropy loss and validation accuracy of training for XY-polarizations respectively, **b** t-SNE plot of the XY polarization training sets for 27.

3.3 Fabrication errors and measurement analysis

Fabrication error is a non-negligible factor, which affects the actual readout accuracy. To clarify this effect, three common fabrication errors caused by height, side-wall angle and line width are simulated and analyzed. Actually, our concern is the relationship between fabrication errors and spectral noise (spectral variations). As mentioned above, we use the 10% spectra noise to compensate the effects of fabrication errors. Therefore, the following analyses are to verify the rationality of the 10% spectral noise, and to explore its limits in counteracting fabrication errors. As a sequence, the ANN for testing is trained using the 10% spectral noise. To test the robustness of the ANN, all spectra are generated only in the x-polarization state.

As shown in Fig. 8, the nanostructure encoded with '001' is as an example to describe the process of error simulation. 3D lithography enables precise control of relative height of structure. Therefore, 10 nm fabrication (10% of a 100 nm etching step) error is introduced into absolute height, as shown in Fig. 8a. The 10 % error of side-wall angle and line width is equally employed, they are 9 degrees and 100 nm respectively, as illustrated in Fig. 8b and Fig. 8c.

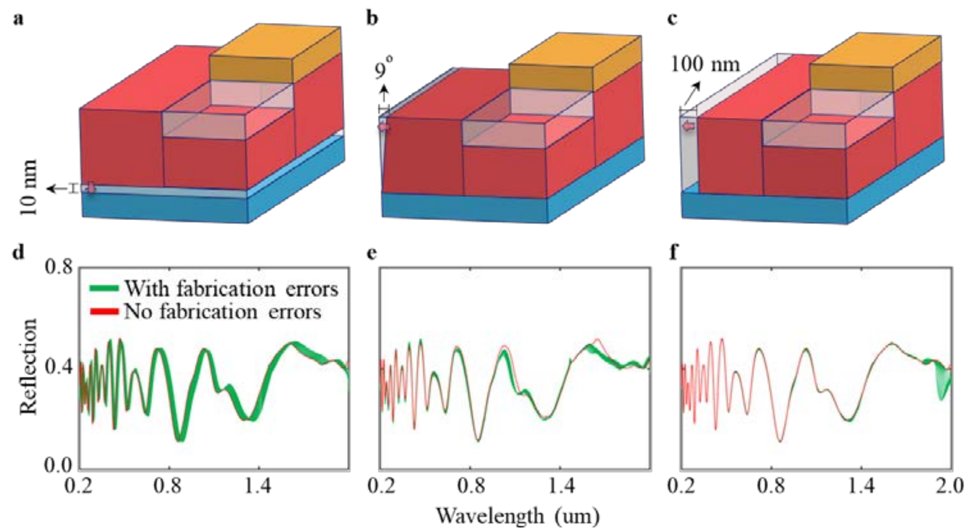

Fig. 8 Three common fabrication errors, the green line is with fabrication errors, the red line is no fabrication errors. **a** fabrication errors of absolute height, **b** fabrication errors of side-wall angle, **c** fabrication errors of line width, **d-f** spectra in X-polarization state for each fabrication error: each error is increased by 1 nm, 1 degree, and 10 nm, respectively to generate 10 spectra.

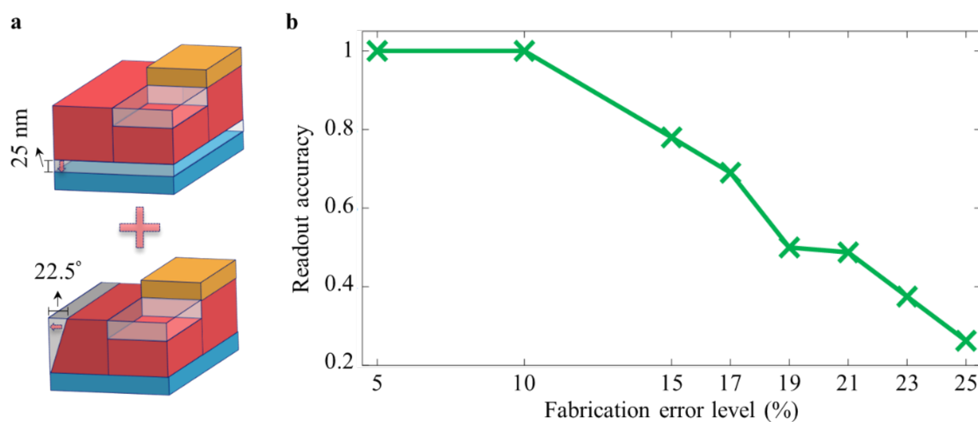

Fig. 9 The readout accuracy of the nanostructures with both height and side-wall angle errors. **a** illustration of both height and side-wall angle errors, **b** readout accuracy variation with extreme fabrication error level.

To further explore the influence of the three fabrication errors on the spectra, they are increased by 1 nm, 1 degree, and 10 nm, respectively. Thus, 10 spectra are generated for each error, as shown in Fig. 8d-f. In Fig. 8d, height changes affect the spectra of full wavelength obviously compare to side-wall angle and line width in Fig. 8e and Fig. 8f. On the contrary, changing in side-wall angle and linewidth, spectra have slight variations only in part of the wavelength range. It is worth noting that the extent of influence of the three errors on the spectral variation is height>side-wall angle>line width. This result justifies the strategy of employing Z-direction height variation to store data information.

Furthermore, the influence of the three errors for in 8 data sequences (100 nm-etching) on the spectrum is also investigated, as illustrated in Fig. S3. All spectra with 10% fabrication errors are tested in trained ANN, 100% readout accuracy is obtained. It means that a 10% fabrication errors causes far less spectral noise than 10%. Moreover, the actual fabrication error is hardly not greater than 10%. In other words, 10% spectral noise is sufficient to compensate for spectral variations caused by fabrication errors. Of course, measurement noise is another factor that must be taken into account in this encoding strategy. However, measurement noise differs depending on the actual measurement equipment and environment. Therefore, it is difficult to give specific values through simulation. In practice, spectral noise (spectral variations) caused by measurement noise is usually less than fabrication errors caused. As a result, applying an additional 10% spectral noise to compensate for the measurement noise is reliable. In conclusion, the 20% spectral noise is sufficient to offset the effects of measurement noise and fabrication errors.

To further assess how extreme fabrication errors influence the readout performance, the nanostructures with both height and side-wall angle errors are simulated and analyzed. The effect of line width on spectral variations is weak, which is ignored here. As shown in Fig. 9a, simultaneous application of two fabrication errors to the same nanostructure. Here the nanostructure encoded with '001' is as an example to describe the process. Given a fabrication error limit of 25%, the corresponding height and side-wall angle variations are 22.5° and 25 nm, respectively. The 8 data sequences (100 nm-etching) with extreme fabrication errors are tested in trained ANN, the readout accuracy with changing extreme fabrication errors is shown in Fig. 9b. When the error increases from 5% to 10%, the readout accuracy can still be maintained at 100%. And the readout accuracy for 15% fabrication errors is still a reasonable 79%. Readout accuracy starts to drop significantly at errors around 17%. When the error is between 19%-21%, the readout accuracy can only reach about 50%. Continue to increase the error to 25%, the readout accuracy will be at an unreasonable value of 26%. It could be improved by combining the spectra of wavelength and angle. From the analyses, the 10% spectral noise still completely offsets the effects of spectral variations, even if considering 10% extreme fabrication errors.

4 The higher storage density

To evaluate the robustness of the recording strategy at higher storage densities, we validated it in higher etching depth. As shown in Fig. 10a, four structures with 10 grayscales are encoded based on the different etching depths. There is a grayscale change between each structure, it means more similarity between the spectra, providing greater difficulty for readout scheme. As a result, the spectra of four-structure configuration preform highly consistent in full wavelength and angle range, as illustrated in Fig. 10b and Fig. 10c. The readout accuracy for 30 training epochs is shown in Fig. 11a, and it reaches 100% when the training epoch is 4. Hence the corresponding t-SNE plot has clear separation boundaries, as shown in Fig. 11b. Similarly, readout accuracy of the reduced wavelength- and wavelength & angle-dependent spectra are analyzed, as shown in in supplementary Fig. S4. This attempt makes it possible to

use higher grayscale structures to achieve higher density storage. The theoretical gray level in 3D lithography can reach up to 4096, it means that 4096 heights can be etched on Si layer in single unit, according to different photoresist heights. Therefore, the number of encoded data sequences in single unit can reach 4096. In practice, it can be reached by increasing the photoresist thickness and reducing the etching depth. Each nanostructure has three units enable coding data information, which means that ~68×10^{9} ($4096\times4096\times4096$) data information storage can be realized per $2\times2\times40.95$ μm (increasing the photoresist thickness to 40.95 μm, reducing etching depth to 10 nm) using the proposed storage strategy.

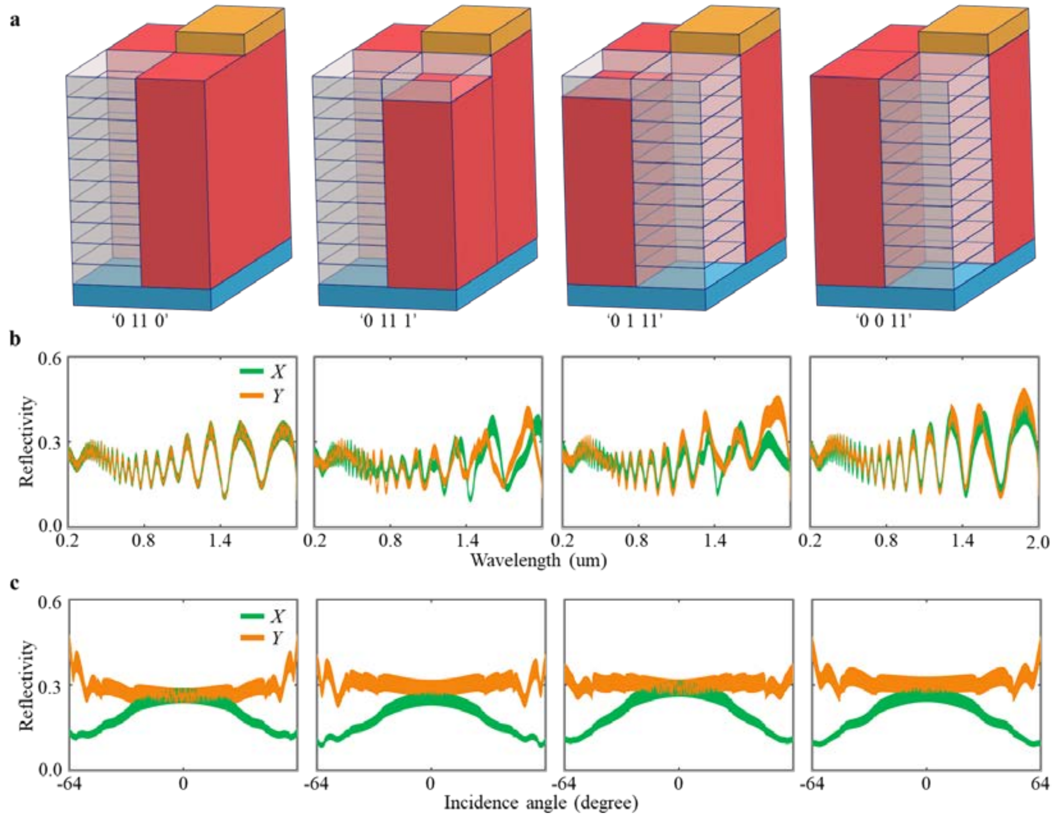

Fig. 10 Encoding four structures with 10 grayscales based on the 1 μm-etching depth. **a** the geometries of four structures, **b** simulated wavelength-dependent spectra for 10-grayscales structures, **c** b simulated angle-dependent spectra for 10-grayscales structures.

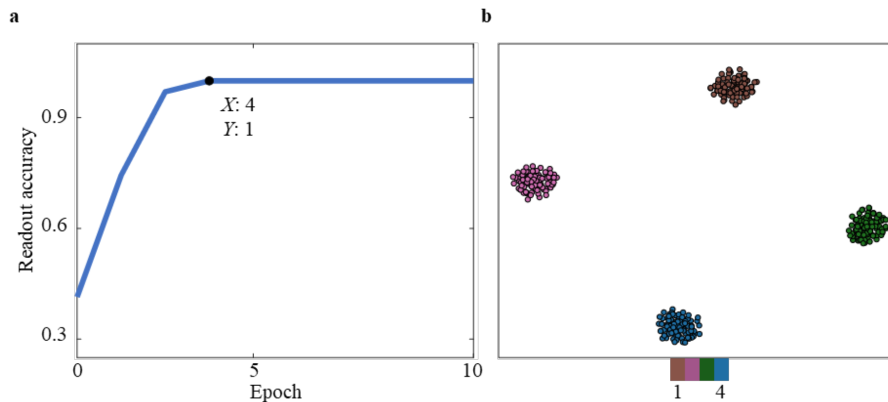

Fig. 11 Training quality and readout accuracy of the ANN trained on full wavelength- and angle-dependent spectra for 10-grayscales structures. **a** readout accuracy of training on full spectra, **b** t-SNE plot of training on full spectra, **c** readout accuracy of network trained on reduced wavelength- and angle-dependent spectra.

4 Conclusions

In this work, a strategy for encoding data information using silicon nanostructures is proposed, inspired by the distinction of reflection spectral discovered in 3D lithography. It is superior to the 2D recording method due to extra encoding data information with 3D recording. Combined with machine-learning method to retrieve the data encoded by the nanostructures, high-density and high-accuracy data information storage can be realized.

Using ANN to retrieve the data encoded by the structures, after 11 and 7 epochs of training, the network can achieve 100% readout accuracy of 8 and 27 sequences, respectively. Moreover, the well-separated t-SNE plot have obtained, to evaluate the distinctiveness of different structures.

To address the similarity of the X and Y polarization spectra due to structural symmetry, a recording method combining wavelength- and angle-dependent spectra was proposed. Using this combining method, the training epoch to reach 100% readout accuracy on both datasets (8 and 27) is reduced by 27% and 29%, respectively, compared with using wavelength spectrum alone.

We train the ANN using reduced spectra information to assess the limit of the amount of data required. When the step size is 50, the corresponding number of selected spectra 25, the readout accuracy of the 27 data sequences can reach 99.7%.

To evaluate the robustness of the readout strategy at higher storage densities, we selected four 10-gray-scale structures with only one gray-scale variation from each other to train the ANN. Even though the resulting spectral information is extremely similar, the network accomplishes the readout with 100% accuracy after 30 training epochs. Using the reduced wavelength and angle-dependent spectra, a high readout accuracy of 98% can be achieved when selecting the number of wavelengths and angles to 18, increasing it to 21 increases the accuracy to 100%.

The proposed 3D optical storage strategy can theoretically achieve a high storage density of ~68×10^6 ($4096\times4096\times4096$) data per $2\times2\times40.96$ μm, which provides a guidance for high-density optical storage research.

Acknowledgements:

This work was supported by the National Key R&D Program of China, under Grant No. 2019YFB1704600; the Hubei Provincial Natural Science Foundation of China, under Grant No. 2020CFA032.

Data Availability

The data that support the findings of this study are available from the corresponding author upon reasonable request.

Reference

[1] Gu M, Li X, Cao Y. Optical storage arrays: a perspective for future big data storage. Light Sci Appl 2014;3:e177–e177.

[2] Gu M, Zhang Q, Lamon S. Nanomaterials for optical data storage. Nat Rev Mater 2016;1:1–14.

[3] Satoh I, Ohara S, Akahira N, Takenaga M. Key technology for high density rewritable DVD (DVD-RAM). IEEE Trans Magn 1998;34:337–42.

[4] Shida N, Higuchi T, Hosoda Y, Miyoshi H, Nakano A, Tsuchiya K. Multilayer optical read-only-memory disk applicable to blu-ray disc standard using a photopolymer sheet with a recording capacity of 100 GB. Jpn J Appl Phys 2004;43:4983.

[5] Li X, Cao Y, Gu M. Superresolution-focal-volume induced 3.0 Tbytes/disk capacity by focusing a radially polarized beam. Opt Lett 2011;36:2510–2.

[6] Xu D, Hu H, He L. Multi-wavelength and multi-level optical storage based on photochromic materials. Seventh Int. Symp. Opt. Storage (ISOS 2005), vol. 5966, SPIE; 2005, p. 40–4.

[7] Xu D. Multi-dimensional optical storage. Springer; 2016.

[8] Liu T, Zhang L, Sun J, Zhong Y, Wang Z, Guo X, et al. Optical properties of dithienylethene and its applications in super-resolution optical storage. Chinese J Lasers 2018;45:903001.

[9] Riesen N, Pan X, Badek K, Ruan Y, Monro TM, Zhao J, et al. Towards rewritable multilevel optical data storage in single nanocrystals. Opt Express 2018;26:12266–76.

[10] Zeng BJ, Ni RW, Huang JZ, Li Z, Miao XS. Polarization-based multiple-bit optical data storage. J Opt 2014;16:125402.

[11] Mottaghi MD, Dwyer C. Thousand-fold increase in optical storage density by polychromatic address multiplexing on self-assembled DNA nanostructures. Adv Mater 2013;25:3593–8.

[12] Psaltis D, Burr GW. Holographic data storage. Computer (Long Beach Calif) 1998;31:52–60.

[13] Novotny L, Hecht B. Principles of nano-optics. Cambridge university press; 2012.

[14] Lee H-E, Kim RM, Ahn H-Y, Lee YY, Byun GH, Im SW, et al. Cysteine-encoded chirality evolution in plasmonic rhombic dodecahedral gold nanoparticles. Nat Commun 2020;11:1–10.

[15] Kuzyk A, Schreiber R, Fan Z, Pardatscher G, Roller E-M, Högele A, et al. DNA-based self-assembly of chiral plasmonic nanostructures with tailored optical response. Nature 2012;483:311–4.

[16] Kuznetsov AI, Miroshnichenko AE, Brongersma ML, Kivshar YS, Luk'yanchuk B. Optically resonant dielectric nanostructures. Science (80-) 2016;354:aag2472.

[17] Park C-S, Shrestha VR, Yue W, Gao S, Lee S-S, Kim E-S, et al. Structural color filters enabled by a dielectric metasurface incorporating hydrogenated amorphous silicon nanodisks. Sci Rep 2017;7:1–9.

[18] Cui Y, Phang IY, Hegde RS, Lee YH, Ling XY. Plasmonic silver nanowire structures for two-dimensional multiple-digit molecular data storage application. Acs Photonics 2014;1:631–7.

[19] El-Rabiaey MA, Areed NFF, Obayya SSA. Novel plasmonic data storage based on nematic liquid crystal layers. J Light Technol 2016;34:3726–32.

[20] Wang L, Rho Y, Shou W, Hong S, Kato K, Eliceiri M, et al. Programming nanoparticles in multiscale: optically modulated assembly and phase switching of silicon nanoparticle array. ACS Nano 2018;12:2231–41.

[21] Jung C, Yang Y, Jang J, Badloe T, Lee T, Mun J, et al. Near-zero reflection of all-dielectric structural coloration enabling polarization-sensitive optical encryption with enhanced switchability. Nanophotonics 2021;10:919–26.

[22] Liu D, Tan Y, Khoram E, Yu Z. Training deep neural networks for the inverse design of nanophotonic structures. Acs Photonics 2018;5:1365–9.

[23] Li X, Cao Y, Tian N, Fu L, Gu M. Multifocal optical nanoscopy for big data recording at 30 TB capacity and gigabits/second data rate. Optica 2015;2:567–70.

[24] Wiecha PR, Lecestre A, Mallet N, Larrieu G. Pushing the limits of optical information storage using deep learning. Nat Nanotechnol 2019;14:237–44.

[25] Cao L, Fan P, Barnard ES, Brown AM, Brongersma ML. Tuning the color of silicon nanostructures. Nano Lett 2010;10:2649–54.

[26] Wiecha PR, Arbouet A, Girard C, Lecestre A, Larrieu G, Paillard V. Evolutionary multi-

objective optimization of colour pixels based on dielectric nanoantennas. Nat Nanotechnol 2017;12:163–9.

[27] Abiodun OI, Jantan A, Omolara AE, Dada KV, Mohamed NA, Arshad H. State-of-the-art in artificial neural network applications: A survey. Heliyon 2018;4:e00938.

[28] Shimobaba T, Kuwata N, Homma M, Takahashi T, Nagahama Y, Sano M, et al. Convolutional neural network-based data page classification for holographic memory. Appl Opt 2017;56:7327–30.

[29] Albawi S, Mohammed TA, Al-Zawi S. Understanding of a convolutional neural network. 2017 Int. Conf. Eng. Technol., Ieee; 2017, p. 1–6.

[30] Van der Maaten L, Hinton G. Visualizing data using t-SNE. J Mach Learn Res 2008;9.